

Training Certifiably Robust Neural Networks Against Semantic Perturbations

Rem Yang¹, Jacob Laurel¹, Sasa Misailovic¹, and Gagandeep Singh^{1,2}

¹ University of Illinois at Urbana-Champaign (UIUC), USA
{remyang2, jlaurel2, misailo, ggnds}@illinois.edu

² VMware Research, USA

Abstract. Semantic image perturbations, such as scaling and rotation, have been shown to easily deceive deep neural networks (DNNs). Hence, training DNNs to be certifiably robust to these perturbations is critical. However, no prior work has been able to incorporate the objective of deterministic semantic robustness into the training procedure, as existing deterministic semantic verifiers are exceedingly slow. To address these challenges, we propose Certified Semantic Training (CST), the first training framework for deterministic certified robustness against semantic image perturbations. Our framework leverages a novel GPU-optimized verifier that, unlike existing works, is fast enough for use in training. Our results show that networks trained via CST consistently achieve both better provable semantic robustness and clean accuracy, compared to networks trained via baselines based on existing works.

Keywords: Certified Robustness · Semantic Perturbations · Provable Training

1 Introduction

Despite the widespread success of deep neural networks (DNNs), particularly in computer vision, they remain surprisingly susceptible to misclassification when small adversarial changes are applied to correctly classified inputs [8, 16]. This phenomenon is especially concerning as DNNs are increasingly being deployed in many safety-critical domains, such as autonomous driving [29] and medical imaging [5]. As a result, many emerging works focus on formally verifying the robustness of neural networks to norm-based adversarial perturbations. For instance, [7, 28, 30, 33] all provide deterministic guarantees that a network will not misclassify any input within some ball (under an ℓ_p -norm) of a given image. However, recent works [3, 4, 10, 13, 21] have shown that *semantic perturbations* – which capture real-world artifacts like scaling and changes in contrast – can also easily deceive DNNs. Furthermore, the ℓ_p -norm threat model does not adequately capture these realistic conditions [3, 21].

Limitations of Existing Work. Prior works [9, 23, 31, 32] incorporate verification explicitly into the training loop so that the trained networks become easier



Fig. 1. Visualization of the semantic perturbations we analyze.

Top: original image with rotation, translation, scale, and shear perturbations.

Bottom: contrast, brightness, and YUV color space perturbations.

to verify. Typically, this task is accomplished by formulating a loss function that strikes a balance between the desired formal guarantees (i.e., high certified robustness) and clean accuracy (i.e., the network’s accuracy on the original dataset). To ensure quick loss computation over a large set of training images, interval bound propagation (IBP) [9, 23] is the most popular for expressing formal guarantees. However, despite the success of existing certified training methods, they are tailored to train networks robust against norm-based perturbations, and are not effective in training networks robust against semantic perturbations.

Challenges. Training networks to be certifiably robust against semantic perturbations carries multiple challenges that do not arise with norm-based perturbations. First, semantic perturbations, such as those in Fig. 1, are more difficult to formally reason about, as the adversarial region cannot be represented as a symbolic formula encoding a convex shape. Second, computing a sound over-approximation of such a region requires significant additional computation. Existing deterministic verifiers for semantic perturbations [2, 24] are exceedingly slow, while other semantic robustness verifiers [6, 20] only provide probabilistic guarantees, which may be inadequate for safety-critical applications. Since provable training requires computing certified bounds over large amounts of training data, incorporating existing verifiers into training is prohibitively expensive.

Contributions. To address the outlined challenges, we propose Certified Semantic Training (CST), a framework for training neural networks that are deterministically robust to semantic perturbations. A key insight underlying CST is that for certified training to semantic perturbations to be practical, semantic robustness verification must be highly scalable (which prior approaches were not). Hence, we first develop a novel method to perform fast semantic robustness certification that is orders of magnitude faster than the state-of-the-art. Building on this, we formulate a computationally efficient loss function that incorporates our semantic robustness verifier into the training procedure. We empirically evaluate our method on the MNIST [19], CIFAR10 [15], and Tiny-ImageNet [18] datasets to demonstrate CST’s effectiveness. Though no prior training works exist for our specific setting, we adapt norm-based IBP [9] and PGD [22] training to our domain as baselines.

Our results show that CST-trained networks significantly outperform the baseline approaches, consistently achieving both better certified robustness and clean accuracy. Furthermore, we are able to certify – for the first time – deterministic robustness against semantic perturbations on entire test sets of 10,000 images, which is more than $50\times$ the number of images over existing works (100 in [2] and 200 in [24]).

2 Background

In this section, we formally describe the relevant background needed for presenting our technical contributions in the next section. We denote a classification neural network, $f: \mathbb{R}^{C \times H \times W} \rightarrow \mathbb{R}^n$, as a function from an $H \times W$ image with C channels to n output classes. We focus on feedforward networks, but our approach is general and applicable to any classification architecture.

Interval Bound Propagation. For each pixel in the input and each neuron in the network, verification with interval bound propagation (IBP) [9] associates an interval containing bounds on its minimum and maximum values. We denote interval variables in bold: e.g., $\mathbf{x} = [\underline{x}, \bar{x}]$ is an interval with \underline{x} and \bar{x} as lower and upper bounds, respectively. A sound verifier propagates intervals through the network from the input layer till the output layer by interpreting network transformations using interval arithmetic. For instance, the output interval for a neuron \mathbf{z} obtained by applying a monotonic activation function $h: \mathbb{R} \rightarrow \mathbb{R}$ (e.g., ReLU) elementwise to input \mathbf{x} is $\underline{z} = h(\underline{x})$, and $\bar{z} = h(\bar{x})$. Intervals can also be propagated through fully connected and convolutional layers by interpreting their affine transformations with interval addition and multiplication. We now introduce the notion of certified robustness.

Definition 1 (Worst-Case Output and General Certified Robustness).

For an image $x \in \mathbb{R}^{C \times H \times W}$ with label y_t and a network f , let the network output for the correct class be denoted as $f_{y_t}(x)$ and for any incorrect class as $f_j(x)$, where $j \in \{1, 2, \dots, n\} \setminus \{y_t\}$. Given a set of perturbed inputs $\mathbf{x} = [\underline{x}, \bar{x}]$, we denote the worst-case output vector as $\hat{f}(\mathbf{x})$, where (interpreting all operations via interval arithmetic) the correct class's entry is its lower bound and all other entries are their upper bounds:

$$\hat{f}_{y_t}(\mathbf{x}) = \underline{f}_{y_t}(\mathbf{x}) \quad \text{and} \quad \hat{f}_j(\mathbf{x}) = \bar{f}_j(\mathbf{x}) \quad (1)$$

We say that f is certifiably robust for \mathbf{x} if, even in the worst case, we can still guarantee that the network classification is correct:

$$y_t = \underset{i}{\operatorname{argmax}} \hat{f}_i(\mathbf{x}) \quad (2)$$

Semantic Perturbations. Many existing works on training networks for certified robustness [9, 23, 31, 32] consider ℓ_∞ perturbations on the input x , where the perturbation bounds are computed as $\mathbf{x} = [x - \epsilon, x + \epsilon]$ (with $\epsilon \in \mathbb{R}_{>0}$ being the radius of the ℓ_∞ ball). In contrast, our work targets semantic perturbations that correspond to alterations of the input image in semantically meaningful ways, versus just altering the raw low-level pixel values as in the ℓ_p -norm threat model. We denote a semantic image perturbation as a function $P: \mathbb{R}^{C \times H \times W} \times \mathbb{R}^p \rightarrow \mathbb{R}^{C \times H \times W}$, which takes an input image and p parameters (e.g., angle of rotation and amount of brightness), then produces the semantically perturbed image. We formally define all the perturbations that we analyze in Appendix A.

Geometric Transformations. As a concrete example, geometric perturbations involve an affine transformation on each pixel’s row and column indices, followed by an interpolation operation. As these operations are performed in the 2D plane, we must interpret the row and column indices as points in \mathbb{R}^2 . Hence, we have functions $\phi_x(j) = j - (W - 1)/2$ and $\phi_y(i) = (H - 1)/2 - i$, which convert i, j pixel indices to x, y coordinates with respect to the center of an $H \times W$ image. Let $T_\theta: \mathbb{R}^2 \rightarrow \mathbb{R}^2$ be an invertible affine transformation (e.g., rotation or translation) parameterized by θ (e.g., rotation angle or amount of horizontal shift). Having converted pixel indices to \mathbb{R}^2 , we compute for each location $(\phi_x(j), \phi_y(i))$ the (real-valued) coordinate that maps to this location under T_θ ; we can obtain this coordinate as $(x', y') = T_\theta^{-1}(\phi_x(j), \phi_y(i))$, where T_θ^{-1} is the inverse transformation. However, as these transformed coordinates may not align exactly with integer-valued pixel indices, we must interpolate. Here, we consider the bilinear interpolation kernel, which is the most popular and yields the best results [2, 12]. For a (single-channel) image $X \in \mathbb{R}^{H \times W}$, the function I used to compute the bilinear interpolation is given in [12] as:

$$I(x', y') = \sum_{n=1}^H \sum_{m=1}^W X_{n,m} \cdot \max(0, 1 - |y' - \phi_y(n)|) \cdot \max(0, 1 - |x' - \phi_x(m)|) \quad (3)$$

Having defined interpolation, we now define the general form of a geometric perturbation for an image X as:

$$X'_{i,j} = I(T_\theta^{-1}(\phi_x(j), \phi_y(i))) \quad (4)$$

where X' is the geometrically perturbed image. For multichannel images, Eq. (4) is applied independently to each channel. Additionally, one can combine multiple different geometric transformations to obtain a composite perturbation, e.g., $T_\theta(x, y) = (T_{\theta_1}^{rotate} \circ T_{\theta_2}^{shear} \circ \dots \circ T_{\theta_n}^{scale})(x, y)$. The full equations for each geometric transformation are given in Eqs. (10)–(13) in Appendix A.

Certified Semantic Robustness. To certify semantic robustness requires computing the bounds on an image x as $\mathbf{x} = P(x, \boldsymbol{\theta})$, where $\boldsymbol{\theta} = [\underline{\theta}, \bar{\theta}]$ is an interval vector bounding the range of semantic perturbation parameters, and the perturbation function P is interpreted over interval arithmetic. Hence, the worse-case output for semantic perturbations is: $\hat{f}_{y_t}(P(x, \boldsymbol{\theta})) = \underline{f}_{y_t}(P(x, \boldsymbol{\theta}))$ and $\hat{f}_j(P(x, \boldsymbol{\theta})) = \bar{f}_j(P(x, \boldsymbol{\theta}))$ for $j \in \{1, 2, \dots, n\} \setminus \{y_t\}$. However, for a given range of semantic perturbation parameters $\boldsymbol{\theta}$ for which we wish to verify robustness, the interval width $\bar{\theta} - \underline{\theta}$ may be too large for the direct evaluation of $\hat{f}(P(x, \boldsymbol{\theta}))$ to yield bounds that are precise enough for successful certification. Hence, like other semantic robustness certifiers [2, 24], we employ input splitting. Here, we split the entire range of input parameters into smaller intervals (such that their union is the entire range) and certify each split independently; if verifying all splits succeeds, then certification holds on the entire range. Our certification problem thus becomes the following.

Definition 2 (Certified Robustness for Semantic Perturbations). For an image $x \in \mathbb{R}^{C \times H \times W}$ with label y_t , a network f , a perturbation function P , and a set of K disjoint interval vectors $S = \{\theta_1, \theta_2, \dots, \theta_K\}$ where $\bigcup S = \theta$, we say that f is certifiably robust for $P(x, \theta)$ if:

$$y_t = \underset{i}{\operatorname{argmax}} \hat{f}_i(P(x, \theta_k)) \quad \forall k \in \{1, 2, \dots, K\} \quad (5)$$

3 Certified Semantic Training

We now define the new training algorithm robust to semantic perturbations.

3.1 Loss Objective

The key to incorporating robustness guarantees into training lies in formulating certification as part of the loss function. Since \hat{f} represents the worst-case certifier output under a range of perturbed inputs, we can use it in the training loss to penalize networks that are not provably robust. Importantly, to take into account input splitting during certification (which is unique to the setting of semantic perturbations), we formulate our training loss to enforce *local* semantic robustness at the level of individual input splits. Furthermore, to still certify the network across the entire desired range $\theta = [\underline{\theta}, \bar{\theta}]$, we enforce this local property across all splits. Similar to other works on certified training, we also need to enforce high *clean* accuracy. Hence, we arrive at the following loss formulation.

Definition 3 (Ideal Loss Function). For a network f , an input x with label y_t , and K partitioned ranges of semantic perturbation parameters $\{\theta_k\}$ where $\bigcup_{k=1}^K \theta_k = \theta$, we can compute the ideal loss L as:

$$L(x, y_t) = \kappa \cdot \ell(f(x), y_t) + \left(\frac{1 - \kappa}{K}\right) \cdot \sum_{k=1}^K \ell(\hat{f}(P(x, \theta_k)), y_t) \quad (6)$$

where ℓ can be any classification loss function (we use the cross-entropy loss) and $\kappa \in [0, 1]$ governs the relative weighting between the clean accuracy and semantic robustness terms (with higher κ prioritizing clean accuracy).

In practice, the loss in Eq. (6) is too computationally expensive, since the runtime scales linearly with the number of splits, which often needs to be large to ensure precise certification. As a remedy, we enforce the robustness property *stochastically* using data augmentation in conjunction with a randomized sampling of interval splits, which we describe below.

Definition 4 (Tractable Loss Function). For a network f and an input x with label y_t , we uniformly sample a scalar perturbation amount $\theta \sim \mathcal{U}(\underline{\theta}, \bar{\theta})$ and compute a local interval split $\theta_l = [\theta - \nu, \theta + \nu]$ (where ν is a hyperparameter vector governing the interval size of each perturbation parameter). We can then compute the tractable loss L as:

$$L(x, y_t) = \kappa \cdot \ell(f(P(x, \theta)), y_t) + (1 - \kappa) \cdot \ell(\hat{f}(P(x, \theta_l)), y_t) \quad (7)$$

Since we sample a different θ for each mini-batch of training samples, this approach will, on average, effectively enforce local robustness over the entire desired range (hence leading to global robustness). As in prior works [9, 31, 32], we can vary κ with the training iteration, temporally changing the weighting between clean accuracy and robustness. The hyperparameter vector ν is akin to ϵ in the ℓ_∞ -norm case, but it governs the size of a “semantic ball” around an image rather than an ϵ -ball; note that ν is a vector, since the interval size corresponding to each semantic perturbation may be different. We show that this hyperparameter is easy to determine, even *before* training. Finally, while this loss function incorporates only interval bound propagation, it can easily be adapted to other provable training methods like CROWN-IBP [32] by substituting the ϵ -balls in their loss functions with our formulation of local semantic balls.

3.2 Efficient Verification

A key technical challenge arises during the computation of the loss function in Eq. (7): we need to incorporate the verification objective itself into the loss function, but existing verifiers for semantic perturbations [2, 24] are too slow (due to their sequential and CPU-only implementations), particularly for the geometric perturbations that require interpolation. Specifically, their runtime is bottlenecked by the step of computing images’ bounds under semantic perturbations P . Therefore, a novel *GPU-parallelizable* method for computing P over interval bounds is needed to realize our proposed loss function in practice.

For the contrast, brightness, and YUV color space perturbations (Appendix A Eqs. (8) and (9)), parallelizing P is trivial, since the pixel’s perturbed value depends only on its original intensity, and not on its spatial position relative to other pixels. On the other hand, computing fast interval bounds for geometric perturbations necessitates a novel algorithm, as these *do* involve spatial dependencies between pixels. In existing verifiers, Eq. (4) is evaluated sequentially using 4 nested for-loops *for a given image*. Further, for each image we want to certify, the entire analysis needs to be rerun, so the runtime scales linearly with batch size. Thus, this approach quickly becomes prohibitive for training. To this end, we devise a novel method to efficiently parallelize this computation.

Algorithm 1 describes our method for computing fast image interval bounds under geometric transformations. We mathematically decompose the geometric perturbation (Eqs. (3) and (4)) into three parts: **(1)** computing the coordinates of each pixel under inverse transformation T_θ^{-1} , **(2)** computing the interpolation distances $\max(0, 1 - |y' - \phi_y(n)|) \cdot \max(0, 1 - |x' - \phi_x(m)|)$, and **(3)** finally obtaining the resulting interpolated images. Our key insight is that steps **(1)** and **(2)** are solely dependent on the transformation T_θ and the height and width of the images, *not* the image pixel values themselves. Hence, these computations need only be done once for a given transformation range, amortizing the cost for *any* number of images in a batch. We now detail each part. Additionally, we provide a running example of Algorithm 1 in Appendix B.

Algorithm 1 Fast interval geometric transformation.

Input: $X \in [0, 1]^{N \times C \times H \times W}$, a batch of N images with dimension $C \times H \times W$
 T_θ , a geometric transformation with interval parameters θ
Output: $X' \in [[0, 1]^{N \times C \times H \times W}, [0, 1]^{N \times C \times H \times W}]$

- 1: **procedure** MAKEINTERPGRID(H, W, T_θ)
- 2: $(i, j) \leftarrow ([0, 1, \dots, H-1], [0, 1, \dots, W-1])$
- 3: $(x, y) \leftarrow (j - (W-1)/2, (H-1)/2 - i)$ \triangleright compute $(\phi_x(j), \phi_y(i))$
- 4: $(x_g, y_g) \leftarrow (\underbrace{[x^T, x^T, \dots, x^T]^T}_{H \text{ times}}, \underbrace{[y^T, y^T, \dots, y^T]^T}_{W \text{ times}})$ \triangleright create meshgrid of x, y coords; x_g, y_g are $H \times W$
- 5: $(\mathbf{x}', \mathbf{y}') \leftarrow T_\theta^{-1}(x_g, y_g)$
- 6: $(\mathbf{x}', \mathbf{y}') \leftarrow (\mathbf{x}'.\text{reshape}(HW, 1, 1), \mathbf{y}'.\text{reshape}(HW, 1, 1))$ $\triangleright HW \times 1 \times 1$
- 7: $\mathbf{g} \leftarrow \max(0, 1 - |\mathbf{y}' - y_g|) \odot \max(0, 1 - |\mathbf{x}' - x_g|)$ $\triangleright HW \times H \times W$
- 8: $Z \leftarrow \text{count_nonzeros}(\mathbf{g}, \text{dim} = 0)$ $\triangleright HW$
- 9: $\mathbf{g} \leftarrow \text{flatten}(\mathbf{g})$ $\triangleright HWHW$
- 10: $z_i \leftarrow \text{get_nonzero_indices}(\mathbf{g})$ $\triangleright \text{sum}(Z)$
- 11: $\mathbf{V} \leftarrow \mathbf{g}[z_i]$ $\triangleright \text{sum}(Z)$
- 12: $(R_s, C_s) \leftarrow (\lfloor (z_i \bmod HW)/W \rfloor, (z_i \bmod HW) \bmod W)$ $\triangleright \text{sum}(Z)$
- 13: **return** $G \leftarrow (R_s, C_s, \mathbf{V}, Z)$ $\triangleright \mathbf{g}$ in custom sparse representation
- 14: **end procedure**
- 15:
- 16: **procedure** INTERPOLATE(X, G)
- 17: $(R_s, C_s, \mathbf{V}, Z) \leftarrow G$
- 18: $\mathbf{s} \leftarrow \mathbf{V} \odot X[:, :, R_s, C_s]$ $\triangleright N \times C \times \text{sum}(Z)$
- 19: $\mathbf{X}'_f \leftarrow \text{split_and_sum}(\mathbf{s}, \text{dim} = 2, \text{sizes} = Z)$ $\triangleright N \times C \times HW$
- 20: **return** $\mathbf{X}' \leftarrow \mathbf{X}'_f.\text{reshape}(N, C, H, W)$
- 21: **end procedure**

Inverse Coordinates. We first determine the inverse coordinates $(\mathbf{x}', \mathbf{y}') = T_\theta^{-1}(\phi_x(j), \phi_y(i))$ for each (i, j) pixel index, where $0 \leq i < H$ and $0 \leq j < W$ for images with height H and width W . The inverse transformations (shown in Appendix A Eqs. (10)–(13)) are pixelwise, hence this step can immediately be parallelized by defining the matrices $x_g, y_g \in \mathbb{R}^{H \times W}$ where $x_g(i, j) = \phi_x(j)$ and $y_g(i, j) = \phi_y(i)$, then applying T_θ^{-1} over this whole grid of coordinates (lines 1 – 5 in Algorithm 1). Since T_θ^{-1} is parameterized by an interval range of parameters, this inverse transformation and all subsequent arithmetic operations are interpreted via interval arithmetic.

Interpolation Grid and Exploiting Sparsity. For each $(\mathbf{x}', \mathbf{y}')$, we next calculate the terms $\max(0, 1 - |\mathbf{y}' - \phi_y(n)|) \cdot \max(0, 1 - |\mathbf{x}' - \phi_x(m)|)$ in Eq. (3); we call these terms interpolation distances and denote them $\mathbf{d}_{n,m}^{\mathbf{x}', \mathbf{y}'}$. Herein lies a key difference between our interpolation distance formulation and that of sequential implementations. In the sequential case, one need only compute $\mathbf{d}_{n,m}^{\mathbf{x}', \mathbf{y}'}$ for n where $\underline{y}' \leq \phi_y(n) \leq \bar{y}'$ and m where $\underline{x}' \leq \phi_x(m) \leq \bar{x}'$; this is because all other values of n, m will evaluate to a distance of 0. However, these ranges of n, m can be vastly different for each $(\mathbf{x}', \mathbf{y}')$. Therefore, the only way to parallelize the simultaneous computation of these distances for all inverse coordinates is to, for

each $(\mathbf{x}', \mathbf{y}')$, compute $\mathbf{d}_{n,m}^{\mathbf{x}', \mathbf{y}'}$ for all $0 \leq n < H$, $0 \leq m < W$. This is shown in lines 6 – 7 in Algorithm 1; the comments denote the shape of the tensors. We term these computed distances the interpolation grid \mathbf{g} .

However, as alluded to, most of the entries in \mathbf{g} will be 0 (i.e., the degenerate interval $[0, 0]$) – typically more than 99.5% of them. Therefore, we design a *custom sparse tensor representation* of \mathbf{g} so that only the nonzero entries will be multiplied with image pixel values (i.e., computing $X_{n,m} \cdot \mathbf{d}_{n,m}^{\mathbf{x}', \mathbf{y}'}$ only when the distance is nonzero). The first observation is that for each nonzero $\mathbf{d}_{n,m}^{\mathbf{x}', \mathbf{y}'}$, we must know its *location* (i.e., n, m) so that we can multiply its value with the corresponding image pixels in the same location. To do so, we convert \mathbf{g} to COO (coordinate) format, which is a 3-tuple of vectors: \mathbf{V} which stores the values of \mathbf{g} and R_s, C_s which store the values' row and column indices n, m . These steps are shown in lines 9 – 12. The second observation is that once we obtain all the summands $\mathbf{s}_{n,m}^{\mathbf{x}', \mathbf{y}'} = X_{n,m} \cdot \mathbf{d}_{n,m}^{\mathbf{x}', \mathbf{y}'}$, we need to know which of them contribute to the same pixel (i.e., have the same \mathbf{x}' and \mathbf{y}') and thus should be summed together; this is non-trivial since the grid values have been flattened into a vector. Hence, on line 8, we store an added piece of information: a vector Z that records the number of nonzero interpolation distances for each $(\mathbf{x}', \mathbf{y}')$.

Obtaining Interpolated Images. Given a sparse representation of the interpolation grid $(R_s, C_s, \mathbf{V}, Z)$, we can now efficiently interpolate across an entire batch of images $X \in [0, 1]^{N \times C \times H \times W}$. For all batch and channel dimensions, we obtain the pixel values at locations corresponding to the interpolation distances in \mathbf{V} (by indexing the last two dimensions of X with R_s, C_s) and elementwise multiply with \mathbf{V} to obtain \mathbf{s} , which contains the values of all summands across all pixels (line 18). Now, to recover the final pixel values, we need to sum the terms belonging to the same pixel (i.e., the $\mathbf{s}_{n,m}^{\mathbf{x}', \mathbf{y}'}$ that have the same \mathbf{x}', \mathbf{y}') together. Here, we split the last dimension of \mathbf{s} into HW chunks $\{c_i\} = \{c_1, c_2, \dots, c_{HW}\}$, where each c_i has length Z_i ; then, each chunk's sum is exactly the final interpolated pixel value (line 19). Finally, since this last dimension has been flattened to take advantage of sparsity, we reshape it back to $H \times W$ to obtain the final interpolated images (line 20).

4 Evaluation

We evaluate the effectiveness of CST over multiple datasets, semantic perturbations, and against several training methods. We implemented CST atop PyTorch [26] and use `auto_LiRPA` [31] as a sound verifier to propagate perturbation bounds through neural networks.

4.1 Experimental Setup

Datasets and Architectures. We evaluate our approach on the MNIST, CIFAR10, and Tiny-ImageNet datasets. For MNIST, CIFAR10, and Tiny-ImageNet, we use convolutional neural network architectures with 4, 5, and 7 layers, respectively. Details are in Appendix C.1.

Perturbations. We provide the full list of semantic perturbations we analyze in Appendix A. For the geometric, contrast, and brightness perturbations, we use the same range of parameters as DeepG [2], since these represent the state-of-the-art. We denote $R(\varphi)$ a rotation of $\pm\varphi$ degrees; $T_x(h)$ and $T_y(v)$ a translation of $\pm h$ pixels horizontally and $\pm v$ pixels vertically, respectively; $Sc(\lambda)$ a scaling of $\pm\lambda\%$; $Sh(m)$ a shearing of $\pm m\%$; $C(c)$ a contrast change of $\pm c\%$; and $B(b)$ a brightness change of $\pm b$. For the YUV perturbations, we choose $\frac{2}{773}$ and $\frac{8}{773}$ as interval radii, as an ℓ_∞ ball of size ϵ in the YUV space can be as large as 3.03ϵ in the RGB space. Hence, these correspond to ℓ_∞ balls of radii $\epsilon = \frac{2}{255}$ and $\frac{8}{255}$ (which are standard ranges [9, 32]) for the original RGB images. We denote $YUV(\epsilon)$ a perturbation of *all three* YUV channels, each by $\pm\epsilon$.

Baseline Training Methods. To demonstrate the benefits of CST, we compare CST (using the loss defined in Eq. (7)) with three state-of-the-art baseline methods: (1) data augmentation; (2) augmentation with PGD [22], denoted PGD+A; and (3) augmentation with IBP [9], denoted IBP+A. We select these baselines because, to the best of our knowledge, they are the only training methods utilized in existing works on *deterministic* semantic robustness [2, 24]. For (1), the loss function is simply the cross-entropy loss, with input images augmented according to the perturbations we are trying to certify. For (2), we use PGD to generate adversarial examples of the augmented images. For (3), we employ the IBP loss, with interval ϵ -balls placed around the augmented images.

Training Details. We train all MNIST networks for 100 epochs with a batch size of 256, CIFAR10 networks for 120 epochs with a batch size of 128, and Tiny-ImageNet networks for 160 epochs with a batch size of 128. For training with CST and with the IBP+A baselines, we first train with *only* the cross-entropy loss during a warm-up period. Afterwards, in order to ensure better convergence for the loss, we linearly decay κ from 1 to $\kappa_f = 0.5$ and employ a linear ramp-up schedule to slowly increase the value of ν from 0 up to ν_f (for CST) and ϵ from 0 up to ϵ_f (for IBP+A). We choose the ϵ_f values for IBP+A on MNIST (0.1, 0.2) and CIFAR10 ($\frac{2}{255}$) from [9]. For Tiny-ImageNet, we choose $\epsilon_f = \frac{1}{510}$, which we find yields the best tradeoff between clean and certified accuracy. For PGD+A, we use ℓ_∞ balls of size ϵ_f . More training details are in Appendix C.2.

Parameter Interval Sizes. A key question arises: what value of ν_f (which controls parameters’ interval sizes in our loss) yields the best results? For a perturbation P , we empirically found that selecting values of ν_f such that each image’s average interval width per pixel after applying P is sufficiently small works well. Importantly, these sizes can be determined *before* any training. To do so, we uniformly sample 20 random scalar parameter values θ (where $\theta \sim \mathcal{U}(\underline{\theta}, \bar{\theta})$ as in Eq. (7)) and compute, for all train set images, their average interval width per pixel under perturbation of P with parameters $\theta \pm \nu_f$. For our main results (Sections 4.2–4.5), we select values of ν_f such that this width is about 1/4 to 1/2 the typical size used in ℓ_∞ provable training.

When verifying, we further divide each parameter’s range into splits that are smaller than the sizes used during training (typically by a factor of 1/4 to 1/2), so that certification is more precise. For each experiment, we use the same splits to certify all networks. We provide the specific values of ν_f and certification sizes for all experiments in Table 6 of Appendix C.3.

Metrics. During training, we measure per-epoch runtime and maximum GPU memory usage to study the overhead of our approach; for CST and IBP+A, we only consider the epochs after warm-up (i.e., when we start computing the interval robustness loss term). After training, we measure clean accuracy on the test set, as well as what fraction of all test images are certified to still be correctly classified when perturbed under the range of semantic transformations.

Verification Method. For the semantic robustness verification of *all* methods, we use our optimized interval-domain verifier, as the existing semantic robustness verifiers, DeepG [2] and Semantify-NN [24], are prohibitively slow; these works only certified 100 and 200 images in their respective evaluations, while we certify 10,000 images in our work. As an example, to compute interval bounds for 1,024 images under rotation, our method (Algorithm 1) running on GPU is $15461\times$, $20074\times$, and $42670\times$ faster on MNIST, CIFAR10, and Tiny-ImageNet compared to the state-of-the-art interval verifier [24], which is CPU-only. The end-to-end certification runtimes for all benchmarks are in Table 7 of Appendix D.1.

Hardware. We trained and certified all networks on a machine with a 2.40GHz 24-core Intel Xeon Silver 4214R CPU with 192GB of main memory and one Nvidia A100 GPU with 40GB of memory.

4.2 MNIST Results

For the MNIST dataset, CST consistently attains the highest certified and clean accuracies compared to all baselines, as seen in Table 1. First, the PGD+A and Augmented baselines are not shown, as the certified accuracy is 0% in all cases; this is likely because our interval verifier – while highly scalable – produces overly loose bounds on networks trained without an explicit interval loss term. Over all benchmarks, the respective average certified accuracies are 90.5%, 80.6%, and 72.8% for CST, IBP+A ($\epsilon_f = 0.2$), and IBP+A ($\epsilon_f = 0.1$), and their respective average clean accuracies are 98.8%, 97.7%, and 98.7%. For IBP+A ($\epsilon_f = 0.1$), we observe that while the networks maintains high clean accuracy, they give relatively little certified guarantees. By enlarging the interval bound as in the IBP+A ($\epsilon_f = 0.2$) baseline, certified accuracy improves on average, though at the cost of a significant drop in clean accuracy. For the rotation and translation benchmarks, increasing the interval bound actually hurts certified accuracy – this shows that naively using a larger ℓ_∞ ball does not necessarily yield better results. Our approach, which can supply precise bounds that correspond to the semantic perturbations we are trying to certify, is able to attain substantial certified accuracy with negligible to no loss of clean accuracy.

Table 1. Comparison of training methods on MNIST networks. In addition to the training methods presented below, we also evaluated the baselines of PGD+A ($\epsilon_f = 0.2$), PGD+A ($\epsilon_f = 0.1$), and Augmented. However, networks trained with these methods attain no certified robustness across all benchmarks, and are thus not presented.

Perturbations	Training Method	Certified (%)	Accuracy (%)	Time per epoch (s)	Max GPU memory (MB)
R(30)	CST	91.0	98.8	3.27	116.7
	IBP+A ($\epsilon_f = 0.2$)	80.9	97.3	2.70	116.6
	IBP+A ($\epsilon_f = 0.1$)	81.4	98.7	2.65	116.6
$T_x(2)$, $T_y(2)$	CST	85.9	98.9	3.18	116.7
	IBP+A ($\epsilon_f = 0.2$)	68.6	97.4	2.68	116.6
	IBP+A ($\epsilon_f = 0.1$)	72.9	98.7	2.69	116.6
Sc(5), R(5), C(5), B(0.01)	CST	90.7	98.8	3.38	116.7
	IBP+A ($\epsilon_f = 0.2$)	83.7	98.0	2.73	116.6
	IBP+A ($\epsilon_f = 0.1$)	70.0	98.8	2.69	116.6
Sh(2), R(2), Sc(2), C(2), B(0.001)	CST	94.5	98.7	3.43	116.7
	IBP+A ($\epsilon_f = 0.2$)	89.2	98.0	2.72	116.6
	IBP+A ($\epsilon_f = 0.1$)	67.0	98.7	2.71	116.6

Table 2, which presents the pixel interval widths used for training and certification, shows why this is the case. While the IBP+A baselines for $\epsilon_f = 0.1$ and 0.2 need to place uniform intervals of width 0.2 and 0.4 around every pixel, CST’s average interval size for each pixel is much smaller in comparison. This leads to less over-approximation for CST and hence higher clean accuracy, while still achieving the desired robustness guarantees. Furthermore, the large discrepancy between maximum and average interval widths in Table 2 signifies that we have sufficiently captured the high non-uniformity between different pixels’ intervals induced by semantic perturbations.

The time overhead of CST is low, taking about an extra half-second per epoch, since CST must first compute semantic perturbation bounds before propagating them through the sound verifier. In all cases, the maximum GPU memory usage is comparable between CST and IBP+A training, meaning that the additional computations CST performs to analyze the semantic perturbations add negligible memory overhead, which we attribute to the amortized computation of interpolation distances and the sparsity in its representation (Section 3.2).

4.3 CIFAR10 Results

As seen in Table 3, the results on CIFAR10 demonstrate a similar trend. Again, the PGD+A and Augmented networks do not achieve any certified accuracy. Over all benchmarks, the respective average certified accuracies are 51.2% and 46.9% for CST and IBP+A, and their respective average clean accuracies are 69.1% and 62.8% .

Table 2. Average and maximum pixel interval widths of perturbed images used for training (for CST networks) and in certification (for all networks) on MNIST. Each value in the Training and Certification columns is the average over all train set and test set images, respectively.

Perturbations	Average interval width		Maximum interval width	
	Training	Certification	Training	Certification
R(30)	0.06559	0.03652	0.6991	0.4302
$T_x(2)$, $T_y(2)$	0.07383	0.04067	0.5666	0.3274
Sc(5), R(5), C(5), B(0.01)	0.09978	0.06574	0.8173	0.5822
Sh(2), R(2), Sc(2), C(2), B(0.001)	0.08656	0.05272	0.8340	0.5953

The training time per epoch is slightly longer for CST than for IBP+A training; the overhead is about 0.2 seconds per epoch for the YUV perturbations and half a second per epoch for the geometric transformations. Computing geometric bounds takes longer, since it involves interpolation. The memory usage from CST training is comparable in all cases to IBP+A.

The pixel interval widths under perturbation for CIFAR10 (shown in Table 8 of Appendix D.2) also exhibit a similar trend: CST can use widths that are smaller or similar in size than that used by IBP+A (leading to higher clean accuracy), while simultaneously capturing the large intervals caused by the non-uniformity of semantic perturbations (leading to higher certified accuracy).

Finally, even though the semantic perturbations we certify are complex, the certified accuracies we achieve are better than those of other interval-only certified training works (which study the simpler ℓ_∞ case), where certified accuracies range from 32 – 50% [9]. While the clean accuracies for CST are in the 63 – 74% range, these are also typical for *certified* networks (where clean accuracies typically range from 49 – 71% [9]), as it is well-known that attaining provable robustness can come at a cost in clean accuracy.

4.4 Tiny-ImageNet Results

To demonstrate the scalability of CST, we present results on Tiny-ImageNet in Table 4. We highlight this is the first time that deterministic semantic robustness has been evaluated on any dataset larger than CIFAR10. Since images in this dataset are more complex, we train and certify with respect to smaller perturbations that do not impose substantial distortions (and hence preserve semantic meaning). Across all transformations, CST consistently attains the highest certified accuracy compared to the other training methods. The PGD+A and Augmented baselines again achieve no certified robustness. Over all benchmarks, the respective average certified accuracies are 13.6% and 11.8% for CST and IBP+A, and their respective average clean accuracies are 25.1% and 23.7%.

Table 3. Comparison of training methods on CIFAR10 networks. We also evaluated the baselines of PGD+A and Augmented for all benchmarks. However, networks trained with these methods achieve no certifiability.

Perturbations	Training Method	Certified (%)	Accuracy (%)	Time per epoch (s)	Max GPU memory (MB)
YUV($\frac{2}{773}$)	CST	65.0	74.4	5.59	235.9
	IBP+A	59.4	63.4	5.42	236.8
YUV($\frac{8}{773}$)	CST	54.7	71.0	5.58	235.9
	IBP+A	51.6	63.7	5.40	236.8
R(10)	CST	50.3	71.4	5.86	236.2
	IBP+A	43.3	61.3	5.36	235.7
R(2), Sh(2)	CST	45.0	65.7	5.87	236.2
	IBP+A	41.1	62.7	5.40	235.6
Sc(1), R(1), C(1), B(0.001)	CST	41.0	63.1	5.98	237.5
	IBP+A	38.9	63.0	5.46	234.4

Table 4. Comparison of training methods on Tiny-ImageNet networks. The other baselines of PGD+A and Augmented again achieve no certified robustness.

Perturbations	Training Method	Certified (%)	Accuracy (%)	Time per epoch (s)	Max GPU memory (GB)
Sh(2)	CST	16.5	25.7	37.1	2.23
	IBP+A	13.6	23.9	34.8	2.23
Sc(2)	CST	13.3	25.3	37.1	2.23
	IBP+A	12.3	23.9	34.8	2.23
R(5)	CST	10.9	24.3	37.5	2.23
	IBP+A	9.6	23.4	34.8	2.23

The average pixel interval widths used by CST for the Tiny-ImageNet benchmarks (shown in Table 9 of Appendix D.2) are nearly identical in size to that of IBP+A. Yet, CST still attains both higher certified and clean accuracy: this is again because CST can effectively enforce highly non-uniform input bounds that precisely correspond to semantic perturbations.

The runtime overhead of CST over IBP+A is small: around two seconds per epoch. In this case, the overhead is larger than that of CIFAR10 and MNIST, since Tiny-ImageNet pictures have larger dimension. Interestingly, CST incurs *zero* memory overhead compared to IBP+A: this is because the memory required to perform interval bound propagation through a larger network already exceeds the memory that our algorithm uses to compute semantic perturbation bounds.

We again note that the certified and clean accuracies of our networks are comparable to other (norm-based) certified training works [31].

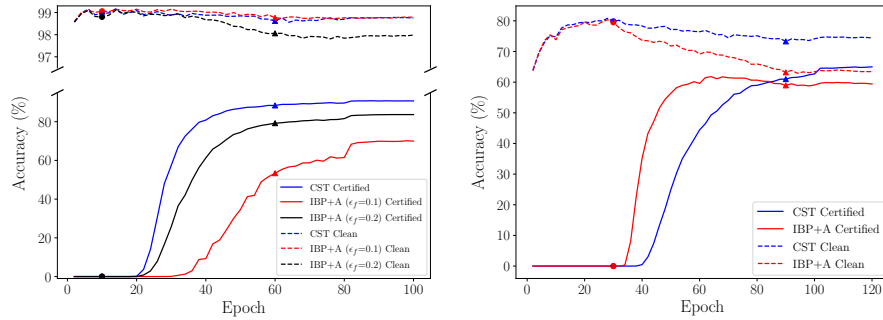


Fig. 2. Certified and clean accuracies as a function of the training epoch for both CST and IBP+A networks. The plot on the left is for the setting of MNIST Sc(5), R(5), C(5), B(0.01) and the plot on the right is for the setting of CIFAR10 YUV($\frac{2}{773}$). $\bullet, \bullet, \bullet$ represent the epoch when we start utilizing the interval loss term (i.e., when we start decreasing κ and increasing ν, ϵ) and $\blacktriangle, \blacktriangle, \blacktriangle$ represent when ν, ϵ have reached the desired interval bound (i.e., when $\nu = \nu_f, \epsilon = \epsilon_f$, and after which only κ is decreasing).

4.5 Evolution of Certifiability and Accuracy

To study how the tradeoff between certifiability and clean accuracy evolves during training, we plot the certified and clean accuracies for CST and IBP+A as a function of the training epoch. In Fig. 2, we show these results for both the MNIST networks perturbed by scaling, rotation, contrast, and brightness and the CIFAR10 networks perturbed in the YUV color space.

For the MNIST experiments in Fig. 2, we notice that for CST, the clean accuracy drops only slightly while the certified accuracy increases sharply (before stabilizing), hence both are attainable. In contrast, the IBP+A ($\epsilon_f = 0.1$) training has negligible clean accuracy decrease, but significantly weaker certified accuracy. For IBP+A ($\epsilon_f = 0.2$), there is a relatively large drop in clean accuracy, and it *still* attains less certified accuracy than CST. These results highlight the fact that in IBP+A training, high clean accuracy and high certified accuracy are mostly mutually exclusive; in contrast, CST can achieve a better tradeoff. Additionally, CST converges to a better result faster than IBP+A, and the training process is quite stable.

For the CIFAR10 experiments in Fig. 2, the same overall trend holds. While IBP+A training needs to trade off significant clean accuracy for certifiability, CST can simultaneously achieve both much higher clean *and* certified accuracy. Another observation is that decreasing κ (i.e., weighing the robustness term more) for the IBP+A baseline does not necessarily improve certifiability against semantic perturbations, as shown by the slightly decreasing certified accuracy after epoch 60; this is problematic since it can be difficult to know when to stop training the network. Conversely, since our loss function precisely captures properties of semantic perturbations, we can be sure that lower κ values will lead to greater certifiability.

Table 5. Variation of clean and certified accuracy as a function of ν_f . Each entry is a tuple of (clean accuracy, certified accuracy). c is the certification interval size, ν_o is the value of ν_f used in previous benchmarks, and $g = \nu_o - c$. We denote CIFAR10 as C and MNIST as M .

ν_f	C : R(10)	C : R(2), Sh(2)	C : YUV($\frac{2}{773}$)	M : Sc(5), R(5), C(5), B(0.01)
c	77.0, 44.8	69.6, 38.6	77.0, 60.5	99.0, 87.8
$c + \frac{g}{2}$	73.6, 50.2	67.3, 43.9	75.7, 64.1	98.9, 89.9
ν_o	71.4, 50.3	65.7, 45.0	74.4, 65.0	98.8, 90.7
$\nu_o + \frac{g}{2}$	69.9, 50.7	63.4, 45.5	73.5, 65.3	98.4, 90.7
$\nu_o + g$	68.8, 49.1	61.9, 45.3	72.5, 65.4	98.2, 90.2

In all cases, the certified accuracy only starts to improve beyond the epoch where the interval loss term is utilized (i.e., where $\kappa < 1$), denoted by the $\bullet, \bullet, \bullet, \bullet$ points. This demonstrates that unless one explicitly penalizes certifiability in the loss function, certified accuracy will likely not increase, which confirms why PGD+A and Augmented networks could not attain any certified accuracy, and why empirical defenses in general are insufficient.

4.6 Effect of Parameter Interval Size

As the size of the local semantic balls (controlled by ν) is a key training hyper-parameter of our loss function in Eq. (7), we conduct an ablation study on how varying ν_f affects the certified and clean accuracies of CST-trained networks. In Table 5, we show these results on three CIFAR10 benchmarks and one MNIST benchmark. In addition to the original value of ν_f used in our benchmarks in Sections 4.2 and 4.3 (termed ν_o), we select four additional settings for ν_f and train with CST for each of these values. We choose the smallest ν_f to be equal to the interval size at certification time, c , and the largest ν_f to be equal to c plus two times the difference between ν_o and c . We certify all networks with the original certification size c .

We can observe that generally, larger values of ν_f lead to increased certified accuracy, at the cost of decreased clean accuracy. CST thus allows one to explicitly tune the tradeoff between these metrics by varying ν_f . The notable exceptions to this trend are the networks with the largest ν_f ; in this case, using a ν_f that is excessively large actually decreases certified robustness. There are diminishing returns to using larger intervals during training: while the certified accuracy increases significantly when using $\nu_f = \nu_o$ compared to $\nu_f = c$, further increasing the size to $\nu_f = \nu_o + \frac{g}{2}$ or above only slightly increases certifiability.

5 Related Work

Certification of semantic perturbations going beyond ℓ_p -norm attacks have recently begun to be studied in the literature [2, 6, 17, 20, 24]. In general, these

semantic perturbations involve modifying the image via geometric transformations (e.g., rotation or scaling) [2, 4], adding visible artifacts (e.g., brightness or contrast) [10, 21], or manipulating the color channels [1, 11, 27], especially in an alternate color space like YUV [1] or HSV [11].

Additionally, while techniques for provable training have been studied before in prior work [9, 23, 31, 32], to the best of our knowledge, there are no provable training frameworks designed specifically for these aforementioned semantic perturbations. This in part stems from the fact that existing deterministic verifiers for semantic perturbations, DeepG [2] and Semantify-NN [24], cannot scale to a large enough number of images needed for training; furthermore, TSS [20] and Fischer et al. [6] only give probabilistic guarantees, whereas our work focuses on deterministic guarantees which *always* hold.

While some works have focused on scaling verifiers [25, 31], none of these have specifically targeted semantic robustness; hence, there are no (GPU-accelerated) deterministic verifiers for semantic perturbations that are efficient enough for use in training.

6 Conclusion

We proposed Certified Semantic Training (CST), a training formulation that improves the certified robustness of neural networks with respect to semantic perturbations. Our experiments on the MNIST, CIFAR10, and Tiny-ImageNet datasets showed that CST consistently attains both better certified semantic robustness and clean accuracy than existing state-of-the-art provable training methods, without substantial training runtime or memory overhead.

References

1. Aydin, A., Sen, D., Karli, B.T., Hanoglu, O., Temizel, A.: Imperceptible adversarial examples by spatial chroma-shift. In: Proc. International Workshop on Adversarial Learning for Multimedia (AdvM). pp. 8–14 (2021)
2. Balunovic, M., Baader, M., Singh, G., Gehr, T., Vechev, M.: Certifying geometric robustness of neural networks. In: Proc. Neural Information Processing Systems (NeurIPS). pp. 15287–15297 (2019)
3. Dreossi, T., Jha, S., Seshia, S.A.: Semantic adversarial deep learning. In: Proc. International Conference on Computer Aided Verification (CAV). pp. 3–26 (2018)
4. Engstrom, L., Tran, B., Tsipras, D., Schmidt, L., Madry, A.: Exploring the landscape of spatial robustness. In: Proc. International Conference on Machine Learning (ICML). pp. 1802–1811 (2019)
5. Finlayson, S.G., Bowers, J.D., Ito, J., Zittrain, J.L., Beam, A.L., Kohane, I.S.: Adversarial attacks on medical machine learning. *Science* **363**(6433), 1287–1289 (2019)
6. Fischer, M., Baader, M., Vechev, M.: Certified defense to image transformations via randomized smoothing. In: Proc. Neural Information Processing Systems (NeurIPS). pp. 8404–8417 (2020)
7. Gehr, T., Mirman, M., Drachler-Cohen, D., Tsankov, P., Chaudhuri, S., Vechev, M.: Ai2: Safety and robustness certification of neural networks with abstract interpretation. In: Proc. IEEE Symposium on Security and Privacy (SP). pp. 3–18 (2018)
8. Goodfellow, I.J., Shlens, J., Szegedy, C.: Explaining and harnessing adversarial examples. In: Proc. International Conference on Learning Representations (ICLR) (2015)
9. Gowal, S., Dvijotham, K.D., Stanforth, R., Bunel, R., Qin, C., Uesato, J., Arandjelovic, R., Mann, T., Kohli, P.: Scalable verified training for provably robust image classification. In: Proc. IEEE/CVF International Conference on Computer Vision (ICCV). pp. 4842–4851 (2019)
10. Hendrycks, D., Dietterich, T.: Benchmarking neural network robustness to common corruptions and perturbations. In: Proc. International Conference on Learning Representations (ICLR) (2019)
11. Hosseini, H., Poovendran, R.: Semantic adversarial examples. In: Proc. IEEE/CVF Conference on Computer Vision and Pattern Recognition (CVPR) Workshops. pp. 1614–1619 (2018)
12. Jaderberg, M., Simonyan, K., Zisserman, A., Kavukcuoglu, K.: Spatial transformer networks. In: Proc. Neural Information Processing Systems (NeurIPS). pp. 2017–2025 (2015)
13. Kanbak, C., Moosavi-Dezfooli, S.M., Frossard, P.: Geometric robustness of deep networks: analysis and improvement. In: Proc. IEEE/CVF Conference on Computer Vision and Pattern Recognition (CVPR). pp. 4441–4449 (2018)
14. Kingma, D.P., Ba, J.: Adam: A method for stochastic optimization. In: Proc. International Conference on Learning Representations (ICLR) (2015)
15. Krizhevsky, A.: Learning multiple layers of features from tiny images. Tech. rep. (2009)
16. Kurakin, A., Goodfellow, I.J., Bengio, S.: Adversarial examples in the physical world. In: Artificial intelligence safety and security, pp. 99–112. Chapman and Hall/CRC (2018)

17. Laurel, J., Yang, R., Singh, G., Misailovic, S.: A dual number abstraction for static analysis of Clarke Jacobians. *Proc. ACM Program. Lang.* **6**(POPL), 1–30 (2022)
18. Le, Y., Yang, X.: Tiny imagenet visual recognition challenge. CS 231N (2015)
19. LeCun, Y., Bottou, L., Bengio, Y., Haffner, P.: Gradient-based learning applied to document recognition. *Proc. of the IEEE* **86**(11), 2278–2324 (1998)
20. Li, L., Weber, M., Xu, X., Rimanic, L., Kailkhura, B., Xie, T., Zhang, C., Li, B.: Tss: Transformation-specific smoothing for robustness certification. In: *Proc. Conference on Computer and Communications Security (CCS)*. pp. 535–557 (2021)
21. Liu, H.T.D., Tao, M., Li, C.L., Nowrouzezahrai, D., Jacobson, A.: Beyond pixel norm-balls: Parametric adversaries using an analytically differentiable renderer. In: *Proc. International Conference on Learning Representations (ICLR)* (2019)
22. Madry, A., Makelov, A., Schmidt, L., Tsipras, D., Vladu, A.: Towards deep learning models resistant to adversarial attacks. In: *Proc. International Conference on Learning Representations (ICLR)* (2018)
23. Mirman, M., Gehr, T., Vechev, M.: Differentiable abstract interpretation for provably robust neural networks. In: *Proc. International Conference on Machine Learning (ICML)*. pp. 3578–3586 (2018)
24. Mohapatra, J., Weng, T.W., Chen, P.Y., Liu, S., Daniel, L.: Towards verifying robustness of neural networks against a family of semantic perturbations. In: *Proc. IEEE/CVF Conference on Computer Vision and Pattern Recognition (CVPR)*. pp. 244–252 (2020)
25. Müller, C., Serre, F., Singh, G., Püschel, M., Vechev, M.: Scaling polyhedral neural network verification on GPUs. In: *Proc. Conference on Machine Learning and Systems (MLSys)*. pp. 733–746 (2021)
26. Paszke, A., Gross, S., Massa, F., Lerer, A., Bradbury, J., Chanan, G., Killeen, T., Lin, Z., Gimelshein, N., Antiga, L., Desmaison, A., Köpf, A., Yang, E.Z., DeVito, Z., Raison, M., Tejani, A., Chilamkurthy, S., Steiner, B., Fang, L., Bai, J., Chintala, S.: Pytorch: An imperative style, high-performance deep learning library. In: *Proc. Neural Information Processing Systems (NeurIPS)*. pp. 8024–8035 (2019)
27. Shamsabadi, A.S., Sanchez-Matilla, R., Cavallaro, A.: Colorfool: Semantic adversarial colorization. In: *Proc. IEEE/CVF Conference on Computer Vision and Pattern Recognition (CVPR)*. pp. 1151–1160 (2020)
28. Singh, G., Gehr, T., Püschel, M., Vechev, M.: An abstract domain for certifying neural networks. *Proc. ACM Program. Lang.* **3**(POPL), 1–30 (2019)
29. Sitawarin, C., Bhagoji, A.N., Mosenia, A., Chiang, M., Mittal, P.: Darts: Deceiving autonomous cars with toxic signs. *arXiv preprint arXiv:1802.06430* (2018)
30. Weng, T., Zhang, H., Chen, H., Song, Z., Hsieh, C., Daniel, L., Boning, D.S., Dhillon, I.S.: Towards fast computation of certified robustness for relu networks. In: *Proc. International Conference on Machine Learning (ICML)*. pp. 5273–5282 (2018)
31. Xu, K., Shi, Z., Zhang, H., Wang, Y., Chang, K.W., Huang, M., Kailkhura, B., Lin, X., Hsieh, C.J.: Automatic perturbation analysis for scalable certified robustness and beyond. In: *Proc. Neural Information Processing Systems (NeurIPS)*. pp. 1129–1141 (2020)
32. Zhang, H., Chen, H., Xiao, C., Goyal, S., Stanforth, R., Li, B., Boning, D., Hsieh, C.J.: Towards stable and efficient training of verifiably robust neural networks. In: *Proc. International Conference on Learning Representations (ICLR)* (2020)
33. Zhang, H., Weng, T.W., Chen, P.Y., Hsieh, C.J., Daniel, L.: Efficient neural network robustness certification with general activation functions. In: *Proc. Neural Information Processing Systems (NeurIPS)*. pp. 4944–4953 (2018)

A Equations for Semantic Perturbations

We define the equations for all the semantic perturbations that we analyze.

Contrast and Brightness. The cumulative effects of contrast and brightness acting on a pixel $X_{i,j}$ of an image X can be given by the respective contrast and brightness semantic perturbation parameters $c, b \in \mathbb{R}$, as described in [2, 24]:

$$X'_{i,j} = \min(1, \max(0, (1 + c) \cdot X_{i,j} + b)) \quad (8)$$

Color Space Attacks. We study the effect of converting an RGB image to a different color space with different color semantics, then perturbing the image in that space before converting it back to standard RGB values. Specifically, we analyze the effect of perturbing images in the YUV color space (as in [1]) with 3 semantic perturbation parameters $\epsilon_y, \epsilon_u, \epsilon_v \in \mathbb{R}$ (one for each channel):

$$(X'^r_{i,j}, X'^g_{i,j}, X'^b_{i,j})^T = M^{-1} \cdot (M \cdot (X^r_{i,j}, X^g_{i,j}, X^b_{i,j})^T + (\epsilon_y, \epsilon_u, \epsilon_v)^T) \quad (9)$$

where $M = \begin{pmatrix} 0.299 & 0.587 & 0.114 \\ -0.299 & -0.587 & 0.886 \\ 0.701 & -0.587 & -0.114 \end{pmatrix}$ for the YUV color space (other color spaces would use a matrix with slightly different coefficients). In our experiments, we use the same amount of perturbation ϵ for all channels (i.e., $\epsilon = \epsilon_y = \epsilon_u = \epsilon_v$).

Geometric Transformations. For each geometric perturbation, we present the equation for its inverse transform T_θ^{-1} , which is used to instantiate the general form in Eq. (4).

Rotation. Parameterized by an angle $\varphi \in [0, 2\pi]$:

$$T_\varphi^{-1}(x, y) = \begin{bmatrix} \cos \varphi & \sin \varphi \\ -\sin \varphi & \cos \varphi \end{bmatrix} \begin{bmatrix} x \\ y \end{bmatrix} = \begin{bmatrix} x \cos \varphi + y \sin \varphi \\ -x \sin \varphi + y \cos \varphi \end{bmatrix} \quad (10)$$

Translation. Parameterized by an amount of horizontal shift $h \in \mathbb{R}$ and an amount of vertical shift $v \in \mathbb{R}$:

$$T_{h,v}^{-1}(x, y) = \begin{bmatrix} x - h \\ y - v \end{bmatrix} \quad (11)$$

Scaling. Parameterized by a scaling factor $\lambda \in \mathbb{R}, \lambda > -1$:

$$T_\lambda^{-1}(x, y) = \begin{bmatrix} \frac{1}{1+\lambda} & 0 \\ 0 & \frac{1}{1+\lambda} \end{bmatrix} \begin{bmatrix} x \\ y \end{bmatrix} = \begin{bmatrix} x/(1+\lambda) \\ y/(1+\lambda) \end{bmatrix} \quad (12)$$

Shearing. Parameterized by a horizontal shearing factor $m \in \mathbb{R}$:

$$T_m^{-1}(x, y) = \begin{bmatrix} 1 & -m \\ 0 & 1 \end{bmatrix} \begin{bmatrix} x \\ y \end{bmatrix} = \begin{bmatrix} x - my \\ y \end{bmatrix} \quad (13)$$

B Example of Fast Interval Geometric Transformation

We present a running example of Algorithm 1. Here, we consider applying a scaling of $\lambda = \pm 2\%$ to 3×3 images. Per Eq. (12), the inverse transform function for this perturbation is:

$$T_{\lambda}^{-1}(x, y) = \left(\frac{x}{1 + [-0.02, 0.02]}, \frac{y}{1 + [-0.02, 0.02]} \right) = \left(\frac{x}{[0.98, 1.02]}, \frac{y}{[0.98, 1.02]} \right)$$

We color code the diagrams below, so that information belonging to the same pixel location has the same color.

Lines 2 - 4: First, we create a meshgrid of (x, y) coordinates so that the inverse transform of all coordinates can be computed in parallel. We obtain:

$$x_g = \begin{bmatrix} -1 & 0 & 1 \\ -1 & 0 & 1 \\ -1 & 0 & 1 \end{bmatrix} \text{ and } y_g = \begin{bmatrix} 1 & 1 & 1 \\ 0 & 0 & 0 \\ -1 & -1 & -1 \end{bmatrix}$$

Line 5: Now, we apply T_{λ}^{-1} to each entry in x_g, y_g . Note that since T_{λ}^{-1} produces interval coordinates, all subsequent operations need to be interpreted via interval arithmetic. We have:

$$\mathbf{x}' = \frac{x_g}{[0.98, 1.02]} = \begin{bmatrix} [-1.02, -0.98] & [0, 0] & [0.98, 1.02] \\ [-1.02, -0.98] & [0, 0] & [0.98, 1.02] \\ [-1.02, -0.98] & [0, 0] & [0.98, 1.02] \end{bmatrix}$$

$$\mathbf{y}' = \frac{y_g}{[0.98, 1.02]} = \begin{bmatrix} [0.98, 1.02] & [0.98, 1.02] & [0.98, 1.02] \\ [0, 0] & [0, 0] & [0, 0] \\ [-1.02, -0.98] & [-1.02, -0.98] & [-1.02, -0.98] \end{bmatrix}$$

Lines 6 - 7: We can now compute the bilinear interpolation grid (i.e., all interpolation distances). For each $(\mathbf{x}', \mathbf{y}')$ coordinate, we compute $\mathbf{x}' - x_g$ and $\mathbf{y}' - y_g$, which are both 3×3 interval matrices. As there are 9 inverse coordinates, we end up with two $9 \times 3 \times 3$ interval tensors \mathbf{x}_d and \mathbf{y}_d (where the ordering of the first dimension is according to row-major order of \mathbf{x}', \mathbf{y}'). The rest of the operations to compute the interpolation distances are all elementwise; we can thus obtain $\mathbf{g} = \max(0, 1 - |\mathbf{y}_d|) \odot \max(0, 1 - |\mathbf{x}_d|)$, shown below. We omit writing entries that are zero (i.e., the interval $[0, 0]$).

[0.96, 1.00]	[0.00, 0.02]			[0.98, 1.00]				[0.00, 0.02]	[0.96, 1.00]
[0.00, 0.02]	[0.00, 4e-4]			[0.00, 0.02]				[0.00, 4e-4]	[0.00, 0.02]
[0.98, 1.00]	[0.00, 0.02]				[1.00, 1.00]			[0.00, 0.02]	[0.98, 1.00]
[0.00, 0.02]	[0.00, 4e-4]								
[0.96, 1.00]	[0.00, 0.02]				[0.00, 0.02]			[0.00, 4e-4]	[0.00, 0.02]
					[0.98, 1.00]			[0.00, 0.02]	[0.96, 1.00]

As discussed in Section 3.2, we can see that the region of interpolation is significantly different for each pixel, hence in order to parallelize the entire computation across all inverse coordinates, we must interpolate over the entire 3×3 range of (x, y) coordinates for each $(\mathbf{x}', \mathbf{y}')$. However, doing so leads to a lot of sparsity in \mathbf{g} , which we can now exploit. (Note: with larger images, typically more than 99.5% of \mathbf{g} are zero entries; however, since the image dimension in this running example is small, the sparsity is not as great.)

Lines 8 - 12: We now convert \mathbf{g} to our custom sparse format before performing interpolation with image pixels, so that all zero-multiplications may be eliminated. First, we count the number of nonzero entries in each inverse coordinate's matrix:

$$Z = \begin{bmatrix} 4 & 2 & 4 & 2 & 1 & 2 & 4 & 2 & 4 \end{bmatrix}$$

Then, we flatten \mathbf{g} (in row-major order) and store it in a COO (coordinate) format. We thus obtain an interval vector \mathbf{V} that stores all the nonzero interpolation distances, along with integer vectors R_s, C_s which, for each value of \mathbf{V} , stores its corresponding row and column index:

$$\begin{aligned} \mathbf{V} &= \begin{bmatrix} [0.96, 1.00] & [0.00, 0.02] & [0.00, 0.02] & [0.00, 4e-4] & [0.98, 1.00] & [0.00, 0.02] & [0.00, 0.02] & [0.96, 1.00] & [0.00, 4e-4] & [0.00, 0.02] \\ \dots & [0.98, 1.00] & [0.00, 0.02] & [1.00, 1.00] & [0.00, 0.02] & [0.98, 1.00] & [0.00, 0.02] & [0.00, 4e-4] & [0.96, 1.00] & [0.00, 0.02] & [0.00, 0.02] \\ \dots & [0.98, 1.00] & [0.00, 4e-4] & [0.00, 0.02] & [0.00, 0.02] & [0.96, 1.00] \end{bmatrix} \\ R_s &= \begin{bmatrix} 0 & 0 & 1 & 1 & 0 & 1 & 0 & 0 & 1 & 1 & 1 & 1 & 1 & 1 & 1 & 1 & 2 & 2 & 1 & 2 & 1 & 1 & 2 & 2 \end{bmatrix} \\ C_s &= \begin{bmatrix} 0 & 1 & 0 & 1 & 1 & 1 & 1 & 2 & 1 & 2 & 0 & 1 & 1 & 1 & 2 & 0 & 1 & 0 & 1 & 1 & 1 & 1 & 2 & 1 & 2 \end{bmatrix} \end{aligned}$$

This concludes the procedure `MakeInterpGrid()`, and we are now ready to use this information to compute actual interpolated images. Consider a batch of 1000 3×3 RGB images, $X \in [0, 1]^{1000 \times 3 \times 3 \times 3}$. Now, consider the first channel of the first image, $X[0, 0]$, which is a 3×3 matrix (whose values we randomly select for this example):

$$X[0, 0] = \begin{bmatrix} .55 & .50 & .42 \\ .53 & .49 & .51 \\ .56 & .62 & .45 \end{bmatrix}$$

Line 18: We multiply each interpolation distance with the pixel value of $X[0, 0]$ in the corresponding location; this will yield the values of all summands in Eq. (3) across all pixels. To accomplish this, we index the image according to the indices stored in (R_s, C_s) and elementwise multiply these pixel values with \mathbf{V} , obtaining $\mathbf{s} = \mathbf{V} \odot X[0, 0, R_s, C_s]$:

$$\begin{aligned} \mathbf{s} &= \begin{bmatrix} [0.53, 0.55] & [0.00, 0.01] & [0.00, 0.01] & [0.00, 2e-4] & [0.49, 0.50] & [0.00, 0.01] & [0.00, 0.01] & [0.40, 0.42] & [0.00, 2e-4] & [0.00, 0.01] \\ \dots & [0.52, 0.53] & [0.00, 0.01] & [0.49, 0.49] & [0.00, 0.01] & [0.50, 0.51] & [0.00, 0.01] & [0.00, 2e-4] & [0.54, 0.56] & [0.00, 0.01] & [0.00, 0.01] \\ \dots & [0.61, 0.62] & [0.00, 2e-4] & [0.00, 0.01] & [0.00, 0.01] & [0.43, 0.45] \end{bmatrix} \end{aligned}$$

Line 19: Finally, we sum the terms in \mathbf{s} that belong to the same pixel location. In the context of the diagram above, this is summing the entries in \mathbf{s} that are of the same color. In practice, this color information is encoded in the vector Z , which stores, for each pixel location, the number of nonzero interpolation entries; hence, we break \mathbf{s} into contiguous chunks such that the length of chunk i (where $0 \leq i \leq 9$) is given by Z_i , and sum all values in each chunk, obtaining:

$$\mathbf{X}'_f = \begin{bmatrix} [0.53, 0.57] & [0.49, 0.51] & [0.40, 0.44] & [0.52, 0.54] & [0.49, 0.49] & [0.50, 0.52] & [0.54, 0.58] & [0.61, 0.63] & [0.43, 0.47] \end{bmatrix}$$

This vector is then reshaped to a 3×3 matrix, yielding the final pixel values of $X[0, 0]$ under transformation:

$$\mathbf{X}' = \begin{bmatrix} [0.53, 0.57] & [0.49, 0.51] & [0.40, 0.44] \\ [0.52, 0.54] & [0.49, 0.49] & [0.50, 0.52] \\ [0.54, 0.58] & [0.61, 0.63] & [0.43, 0.47] \end{bmatrix}$$

Finally, we remark that this interpolation process is completely independent for each batch and channel. Therefore, to parallelize the interpolation across multiple images and channels, we simply need to index across all batch and channel dimensions when computing \mathbf{s} (i.e., let $\mathbf{s} = \mathbf{V} \odot X[:, :, R_s, C_s]$).

C Additional Experimental Details

C.1 Network Architectures

We detail the network architecture used for each dataset below. We express a convolutional layer as a 4-tuple of (number of filters, kernel size, stride, padding). All layers are followed by a ReLU activation, except for the final output layer.

- **MNIST:** 2 convolutional layers of $\{(32, 4, 2, 1), (64, 4, 2, 1)\}$ followed by 2 linear layers with $\{200, 10\}$ neurons.
- **CIFAR10:** 3 convolutional layers of $\{(32, 3, 1, 1), (32, 4, 2, 1), (64, 4, 2, 1)\}$ followed by 2 linear layers with $\{150, 10\}$ neurons.
- **Tiny-ImageNet:** 5 convolutional layers of $\{(64, 3, 1, 1), (64, 3, 1, 1), (128, 3, 2, 1), (128, 3, 1, 1), (128, 3, 2, 1)\}$ followed by 2 linear layers with $\{512, 200\}$ neurons.

C.2 Additional Training Details

Training Schedules for CST and IBP+A. We warm up for 10 epochs on MNIST and 30 epochs on CIFAR10 and Tiny-ImageNet. We linearly decay κ from 1 to κ_f during training; we use a final value of $\kappa_f = 0.5$, as we noticed that using a smaller value adversely affects clean accuracy with little to no improvement to certifiability. We use a linear ramp-up schedule to slowly increase the value of ν (for CST) from 0 up to ν_f and ϵ from 0 up to ϵ_f (for IBP+A) across 50, 60, and 80 epochs for MNIST, CIFAR10, and Tiny-ImageNet, respectively.

Data Preprocessing and Augmentation. During training, as stated in Section 4.1, we first augment the input images according to the set of semantic perturbations to which we want to be robust. In addition, for CIFAR10 and Tiny-ImageNet, we also perform random horizontal flips and select random crops of 32×32 with padding 4 (for CIFAR10) and random crops of 56×56 (for Tiny-ImageNet). At test time, we use a central crop of 56×56 for Tiny-ImageNet. For all datasets, we normalize input images according to the channel statistics from the train set immediately before the first network layer.

Optimizer. We use the Adam optimizer [14] across all networks. For MNIST and CIFAR10, we choose an initial learning rate of 10^{-3} , which we decay by 0.1 at the 80th and 100th epoch, respectively; for Tiny-ImageNet, we choose an initial learning rate of 5×10^{-4} , which we decay by 0.1 after 120 and 150 epochs. For all networks, we clip gradients at a maximum ℓ_2 -norm of 8.

PGD Settings. For the PGD+A baselines, we perform 40 steps with step size 0.005 and 0.01 (for $\epsilon_f = 0.1$ and 0.2, respectively) for MNIST, 7 steps with step size 0.002 for CIFAR10, and 7 steps with step size 0.0005 for Tiny-ImageNet.

Table 6. Interval sizes of semantic perturbation parameters used during training and certification. For experiments with compositions of perturbations, the sizes are specified in the same order as the perturbations.

Dataset	Perturbations	Perturbation parameter interval size	
		Training ($2\nu_f$)	Certification ($\overline{\theta_k} - \theta_k$)
MNIST	R(30)	2	1
	$T_x(2), T_y(2)$	(0.2, 0.2)	(0.1, 0.1)
	Sc(5), R(5), C(5), B(0.01)	(2, 2, 10, 0.02)	(1, 1, 10, 0.02)
	Sh(2), R(2), Sc(2), C(2), B(0.001)	(2, 2, 2, 4, 0.002)	(1, 1, 1, 4, 0.002)
CIFAR10	$YUV(\frac{2}{773})$	$\frac{1}{4} \cdot \frac{4}{773}$	$\frac{1}{8} \cdot \frac{4}{773}$
	$YUV(\frac{8}{773})$	$\frac{1}{8} \cdot \frac{16}{773}$	$\frac{1}{16} \cdot \frac{16}{773}$
	R(10)	0.02	0.005
	R(2), Sh(2)	(0.04, 0.10)	(0.02, 0.05)
	Sc(1), R(1), C(1), B(0.001)	(0.05, 0.02, 1, 0.002)	(0.025, 0.01, 0.5, 0.002)
Tiny-ImageNet	Sh(2)	$\frac{1}{3} \cdot 0.1$	$\frac{1}{12} \cdot 0.1$
	Sc(2)	$\frac{1}{3} \cdot 0.05$	$\frac{1}{12} \cdot 0.05$
	R(5)	0.01	0.0025

C.3 Parameter Interval Sizes

In Table 6, we show the interval sizes of semantic perturbation parameters that we use during training and certification for all experiments (except Section 4.6). In the Training column, we present the final (i.e., after ramp-up) interval size of each perturbation parameter used during training. Since we enforce a local semantic ball of up to $\pm\nu_f$ in Eq. (7), the interval size of this ball is $2\nu_f$. In the Certification column, we present the interval size of *each split* used during semantic robustness certification for all training methods. For experiments with multiple perturbations, the ordering of the sizes corresponds with the ordering of the transformations in the Perturbations column.

D Additional Results

D.1 Verification Runtimes

Table 7 presents the certification time per image *in milliseconds* on each benchmark. Here, we compute certification time over all 10,000 test images and divide this time by 10,000 to obtain the per-image runtime.

Table 7. Certification runtime per image for all our benchmarks.

Dataset	Perturbations	Certification time per image (ms)
MNIST	R(30)	0.271
	$T_x(2), T_y(2)$	5.853
	Sc(5), R(5), C(5), B(0.01)	0.431
	Sh(2), R(2), Sc(2), C(2), B(0.001)	0.305
	YUV($\frac{2}{773}$)	3.178
CIFAR10	YUV($\frac{8}{773}$)	23.000
	R(10)	21.859
	R(2), Sh(2)	81.961
	Sc(1), R(1), C(1), B(0.001)	333.434
	Sh(2)	8.441
Tiny-ImageNet	Sc(2)	16.744
	R(5)	66.956

D.2 Pixel Interval Widths

In Tables 8 and 9, we present the average and maximum pixel interval widths for each perturbation setting on CIFAR10 and Tiny-ImageNet, respectively. Each value in the Training and Certification columns is the average over all train set and test set images, respectively.

Table 8. Average and maximum pixel interval widths of perturbed images used for training (for CST networks) and in certification (for all networks) on CIFAR10.

Perturbations	Average interval width		Maximum interval width	
	Training	Certification	Training	Certification
$\text{YUV}(\frac{2}{773})$	0.00306	0.00153	0.00392	0.00196
$\text{YUV}(\frac{8}{773})$	0.00609	0.00306	0.00785	0.00392
$\text{R}(10)$	0.00530	0.00135	0.01691	0.00429
$\text{R}(2), \text{Sh}(2)$	0.01788	0.00903	0.05547	0.02820
$\text{Sc}(1), \text{R}(1),$ $\text{C}(1), \text{B}(0.001)$	0.01902	0.01058	0.04920	0.02564

Table 9. Average and maximum pixel interval widths of perturbed images used for training (for CST networks) and in certification (for all networks) on Tiny-ImageNet.

Perturbations	Average interval width		Maximum interval width	
	Training	Certification	Training	Certification
$\text{Sh}(2)$	0.00403	0.00101	0.01628	0.00409
$\text{Sc}(2)$	0.00399	0.00100	0.01454	0.00367
$\text{R}(5)$	0.00430	0.00108	0.01582	0.00396